Spherically polarized vector Bessel vortex beams

Justas Berškys ●* and Sergej Orlov ●†

Center for Physical Sciences and Technology, Coherent Optics Laboratory, Sauletekio ave 3, LT-10257, Vilnius, Lithuania

A different type of Bessel-like vortex beams with their intensity spherically modified by a singular polarization structure is introduced. Conventional vector Bessel-Gaussian beams are either linearly or radially (and azimuthally) polarized and their transverse structure is preserved under propagation. In this work, the Bessel-like beams with a Gaussian envelope are spherically polarized: the electric fields are oriented along the radius vector or along with a combination of meridional and azimuthal vectors. For the implementation of such beams, we investigate their vector spatial spectra. The intensity distribution of the beam can be controlled by a proper choice of parameters such as the cone angles of individual plane-wave components and sizes of Gaussian apertures. In the two limiting cases of axicon angles, spherically polarized Bessel beams form either two optical needles or optical-bottle-like intensity patterns.

I. INTRODUCTION

Laser beam shaping and the formation of exotic structured beams are on a rise nowadays. A good example of structured illumination is a nondiffracting Bessel-Gaussian beam [1,2] which exhibits a long focal line and is well known for its self-reconstructing properties [3,4]. Additional degrees of freedom are achieved in the transverse profiles of nondiffracting beams, which have properties comparable to Bessel-beam properties, with the introduction of the so-called Mathieu-Gaussian [5,6] and parabolic-Gaussian (Weber-Gaussian) [7,8] beams.

Usually, Bessel beams have low angular frequencies, so we consider them as a scalar [9]. However, when the angle of the Bessel cone is large enough, a scalar description is not valid anymore and one needs to introduce a vector description [10]. Then, a Bessel beam becomes nonhomogeneously polarized, and even the longitudinal component of the electric field can appear [11,12]. Under tight focusing conditions, they have a dominating longitudinal component of the electric field [13,14]. This happens naturally in the beam as plane-wave components are nearly perpendicular to the propagation axis when they impinge on the focal spot [15].

Yet another degree of freedom appears if we consider non-monochromatic superpositions of Bessel beams. Under these conditions, there is a possibility to create an optical bullet—a so-called focus wave mode (also known as an X-wave) [16,17]. Fascinatingly, these optical bullets demonstrate not only nondiffracting but also nondispersive properties [18,19]. Nondiffracting focus wave modes were realized at a variety of electromagnetic frequencies—from optical [20] to microwaves [21]. Vector extensions to these scalar solutions are also known [22]. Switching from nondiffracting Bessel beams

to the basis of nondiffracting elliptical or parabolical beams results in nonsymmetrically shaped optical bullets [23,24].

The influence of the nonhomogeneous polarization state of the beam on its structure usually results in polarization singularities [25,26], which are present in the vector beams [27,28]. Various polarization singularities result in such exotic photonic structures like Möbius strips [29–31], photonic wheels [32–34], and various optical ribbon structures [35,36]. They distort the beam profile in the transverse plane by the introduction of an intensity zero, which, as a rule, is cylindrically symmetric both for azimuthally and radially polarized beams [37,38].

For example, radial and azimuthal polarization change the intensity distribution of the fundamental Gaussian mode in the *x-y* plane but do not affect the longitudinal profile. This is the manifestation of the fact that those two polarizations are naturally occurring while using cylindrical coordinates during the separation of variables [9,10] in the wave equation. To this end phase and polarization singularities are mostly two-dimensional objects and their presence induces one-dimensional structures in the beam—dark knots of light [39,40].

Complex polarization states are analyzed and represented using the extended concept of the Poincaré sphere and Stokes parameters, adjusted to the beam's topology [41–43]. Nevertheless, this generalization is mostly valid for paraxial fields because it does not include the longitudinal component of the electric field and is not suitable for the depiction of the three-dimensional (3D) electromagnetic fields. In this case, a generalization of Stokes parameters is introduced [44]. The number of parameters increases from four to nine, so the polarization state cannot be represented on the 3D sphere.

However, within electromagnetics, there are so-called vector spherical multipoles [9,45], which have two orthogonal polarization states [46–48]. In what follows, we will call them spherically polarized: when an electric field is oriented radially (electric multipoles), i.e., along the radius vector

---

*justas.berskys@ftmc.lt
†sergejus.orlovas@ftmc.lt

or meridional—azimuthally (magnetic multipoles) when the electric field has no spherical radial component. Those nonhomogeneous polarizations exhibit some intriguing properties: (a) they are spherically symmetric and (b) they have a so-called doughnut shape [49–51]. Yet another fascinating property of these electromagnetic beams is the fact that, due to the spherical symmetry, the polarization singularity resting inside the beam is pointlike [45].

Polarization singularities and optical vortices have already received recognition as optical spanners [52], tweezers [53], and traps [54]. Optical doughnut beams are considered promising for optical manipulation systems, where structured optical fields are employed to handle small objects [55]. These beams have a zero intensity region at the center of the beam [56]. Optical traps confine not only nanoparticles, but also cells, molecules and atoms [57–60].

In this work, we investigate a Bessel-like beam, with a nonhomogeneous polarization state, which can be classified as spherically polarized [61]. Here, we consider this type of a Bessel beam for two cases with two distinct types of intensity distributions: (1) an optical doughnut, mentioned already, and (2) a structure, which can be called a double needle [4,62]. We present analytical expressions for a spherically polarized Bessel-Gaussian beam, investigate spatial spectrum and its properties, and discuss the evolution of the spatial shape while changing various parameters.

II. SCALAR NONDIFFRACTING BEAMS

Nondiffracting beams are scalar monochromatic solutions of the Helmholtz equation maintaining their transverse intensity profile unchanged during propagation [1,2,5–8]. One of the examples is the Bessel vortex beam, which is defined in cylindrical coordinates as [1,2]

$$E(\rho, \varphi, z, t) = J_m(k_\rho \rho) \exp(im\varphi) \exp[i(k_z z - \omega t)], \quad (1)$$

where J_m is the mth order Bessel function of the first kind, $k_\rho = k \sin \theta_B$, and $k_z = k \cos \theta_B$ are transverse and longitudinal components of the wave vector $\boldsymbol{k}$, θ_B is a half angle of the Bessel cone and characterizes the Bessel beam, ω is the angular frequency of light, t is time, m is the topological charge, which describes the phase-front modulation. Bessel vortex beams are endless in space and their energy is nonintegrable, what makes this type of nondiffracting beams unphysical [1,2].

On the other hand, a Bessel-Gaussian beam represents an example of an apertured nondiffracting beam with finite energy, which maintains its properties over the length of the so-called Bessel zone [1–4]. The complex amplitude of a scalar Bessel-Gaussian beam is obtained in the paraxial approximation from the parabolic diffraction equation

$$E(\rho, \varphi, z, t) = \frac{1}{Z} J_m\left(\frac{k_\rho \rho}{Z}\right) \exp\left(-\frac{\rho^2}{d_0^2 Z}\right) \exp\left(-i \frac{k_\rho^2}{2k} \frac{z}{Z}\right)$$
$$\times \exp(im\varphi + ik_z z - i\omega t), \quad (2)$$

where $Z = 1 + iz/z_0$ and $z_0 = kd_0^2/2$ is the Rayleigh length, and d_0 is the radius of the Gaussian aperture. These expressions are usually considered to be valid only on the paraxial conditions [3,63]. In general, a nonparaxial solution can be

obtained by using a paraxial solution in the context of a Lax series [64,65]. A good question here is whether Eq. (2) describes large half-cone-angle situations. The answer is that, by limiting the range of the Bessel half-cone angles up to 70 degrees, the deviations from an exact solution that occur at larger angles do not influence the main features of the beam [66]. It turns out that the complicated summation of the Lax series can be avoided because, even in the nonparaxial regime, Eq. (2) describes the situation well enough and the main aspects of the findings can be analyzed without loss of generality.

The spatial spectrum of the scalar Bessel-Gaussian beam is given by [67]

$$g(k_r, \phi) = d_0^2/2 \exp\left[-(k_r^2 + k_\rho^2)d_0^2/4\right]$$
$$\times I_m(k_r k_\rho d_0^2/2) \exp(im\phi), \quad (3)$$

where I_m is the modified Bessel function and $k_r = (k_x + k_y)^{1/2}$ is a radial vector in Fourier space. The spatial spectrum of the Bessel-Gaussian beam is a ring of radius k_ρ and has a width of $1/d_0$. When $|m| > 0$, the spectrum is azimuthally modulated with phase modulation of $2\pi m$.

For the sake of clarity we introduce two normalization constants:

$$z_{\mathrm{B}} = \frac{d_0}{\sin(\theta_B)}, \quad D_{\mathrm{B}} = \frac{2.405}{k \sin(\theta_B)}, \quad (4)$$

where the constant z_{B} is the length of the Bessel zone, the constant D_{B} is the characteristic width of the Bessel beam, and the θ_B is the half-angle of the Bessel cone.

III. VECTOR BESSEL BEAMS

Vector beams, which are solutions of the vector wave equation, are obtained from scalar beams by using a vectorization method; see more in Ref. [68]. Two orthogonal electromagnetic vector fields are possible in the free space:

$$\boldsymbol{M}(\boldsymbol{r}) = \nabla \times [\boldsymbol{a} E(\boldsymbol{r})], \quad \boldsymbol{N}(\boldsymbol{r}) = \frac{1}{k} \nabla \times \boldsymbol{M}(\boldsymbol{r}), \quad (5)$$

where $\boldsymbol{a}$ is some nontrivially defined vector [68], $\nabla = \hat{\boldsymbol{e}}_x \partial^2/\partial x^2 + \hat{\boldsymbol{e}}_y \partial^2/\partial y^2 + \hat{\boldsymbol{e}}_z \partial^2/\partial z^2$. When $a = \hat{\boldsymbol{e}}_z$, transverse electric and transverse magnetic electromagnetic fields are obtained. The electric field here is either azimuthally or radially polarized [10]. Linear and circular polarizations can be derived either by a linear superposition of these two modes or by selecting $a = \hat{\boldsymbol{e}}_x$, $a = \hat{\boldsymbol{e}}_y$. In this work, we propose to create a vector Bessel beam with $\boldsymbol{a}$ being not a unit constant vector but a radial vector in a spherical coordinate system:

$$\boldsymbol{a} = \boldsymbol{R} = x\hat{\boldsymbol{e}}_x + y\hat{\boldsymbol{e}}_y + z\hat{\boldsymbol{e}}_z. \quad (6)$$

As noted by Stratton [9], this vector ensures that the field described by Eq. (5) satisfy spherical boundary conditions. In general, the electric field in TE mode $\boldsymbol{M}$ is tangential to the surface of a sphere, and the electric field in TM mode $\boldsymbol{N}$ is normal to the sphere surface; see Fig. 1.

We start with an example of an unapertured Bessel beam and combine Eq. (1) with an Eq. (5). The electric field of the resulting transverse electric mode $\boldsymbol{M}$ consists of the
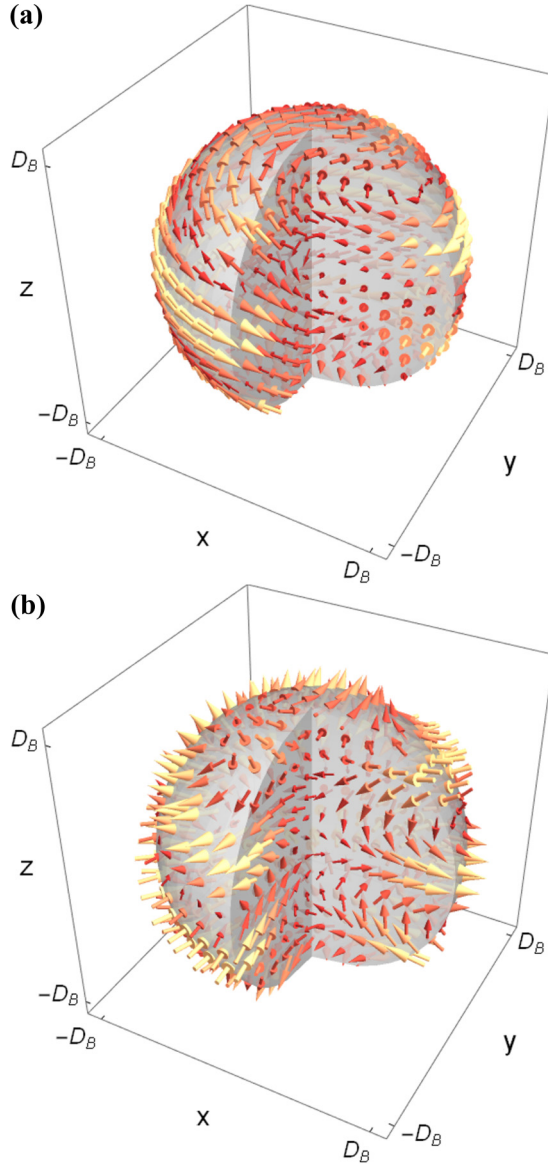
FIG. 1. Schematic depiction of the electric-field orientations in the (a) transverse magnetic and (b) transverse electric spherically polarized Bessel vortices with the topological charge $m = 1$. Electric fields are plotted on the surface of the sphere with radius D_B, which is cut by two half planes at two values of the azimuth ($\phi = 0, \pi/2$).

mth- and $m \pm 1$st-order Bessel vortices whose relative intensities depends on coordinates

$$\boldsymbol{M}_B^m(\rho, \varphi, z, t)$$
$$= \left\{ i \frac{mz}{\rho} J_m(k_\rho \rho)\hat{\boldsymbol{e}}_\rho + [ik_z \rho J_m(k_\rho \rho) - z J_m'(k_\rho \rho)] \right.$$
$$\left. \times \hat{\boldsymbol{e}}_\varphi - imJ_m(k_\rho \rho)\hat{\boldsymbol{e}}_z \right\} e^{ik_z z + im\varphi - i\omega t}. \quad (7)$$

When the topological charge $m = 0$, the electric field has no longitudinal component E_z and is azimuthally polarized in the transverse plane. When $m \neq 0$, the electric field becomes azimuthally and meridionally polarized in the transverse and longitudinal planes, respectively. We observe an appearance

of the intensity minima at the center of the beam. This is the first distinct manifestation of the effect caused by the spherical polarization. When moving further from the center of the beam the transverse intensity distribution is determined solely by higher-order Bessel functions:

$$\lim_{z \to \infty} \boldsymbol{M}_B^m(\rho, \varphi, z, t)$$
$$\approx \frac{zk_\rho}{2}[J_{m-1}(k_\rho \rho)(i - 1) + J_{m+1}(k_\rho \rho)(i + 1)]$$
$$\times (\hat{\boldsymbol{e}}_\rho - \hat{\boldsymbol{e}}_\varphi)e^{ik_z z + im\varphi - i\omega t}. \quad (8)$$

The behavior in one particular case (when $m = 1$) can be revealed from Eq. (7). The electric field in this case at the center of the beam ($\rho \approx 0$) increases linearly with propagation distance $\boldsymbol{M}_B^1(\rho, \varphi, z) \approx zk_\rho(i\hat{\boldsymbol{e}}_x + \hat{\boldsymbol{e}}_y)$. Thus, the electric field is circularly polarized on the z axis, although the topological charge in our derivations was $m = 1$. This situation can be interpreted as orbital-to-spin angular-momentum conversion and was observed for complex source vortices [47].

Yet another way to analyze polarization structures with vortices and topologies is an introduction of a higher-order (hybrid) Poincaré sphere [41–43]. Although spherically polarized Bessel beams exhibit inhomogeneous intensity, so the first Stokes parameter S_0 is not unitary, we can redefine S_1, S_2, and S_3 by normalizing (dividing by S_0) them. See Supplemental Material [69] for an animated depiction of three normalized Stokes parameters representing $\boldsymbol{M}_B^1$ for different points in the x, z plane for different values of θ_B.

On the other hand, the electric field in the transverse magnetic mode is described by the expression for $\boldsymbol{N}_B$:

$$\boldsymbol{N}_B^m(\rho, \varphi, z, t) = \frac{1}{k\rho}\left\{ \left[J_m(k_\rho \rho)(m^2 + \rho^2 k_z^2) + \rho J_m'(k_\rho \rho) \right. \right.$$
$$\left. \times (1 + izk_z)\right]\hat{\boldsymbol{e}}_\rho + m[J_m(k_\rho \rho)(i - k_z z)$$
$$+ i\rho J_m'(k_\rho \rho)]\hat{\boldsymbol{e}}_\varphi + \rho\left[J_m(k_\rho \rho)(2ik_z + zk_\rho^2) \right.$$
$$\left. \left. + ik_z \rho J_m'(k_\rho \rho)\right]\hat{\boldsymbol{e}}_z \right\} e^{ik_z z + im\varphi - i\omega t}. \quad (9)$$

The electric field is spherically polarized with directions predominantly oriented along the radius vector. See Supplemental Material [69] for an animated depiction of three normalized Stokes parameters representing $\boldsymbol{N}_B^1$ for different points in the x, z plane for different values of θ_B.

In both cases, we observe that the very centers of both beams are located on the south pole of the hybrid Poincaré sphere. The polarization state moves to the equator of the sphere for points further away from the center. A cone is observed, on which the polarization state is located on the opposite pole of the Poincaré sphere. The polarization state rapidly moves to the equator in the focal plane. Thus, even for the small angles of θ_B spherically polarized Bessel beams are represented as a set of points on the Poincaré sphere, which are complexly evolving during the diffraction of the beams.

We have performed a similar analysis for conventional radially and azimuthally polarized Bessel beams and polarization states do not change that much during the propagation.
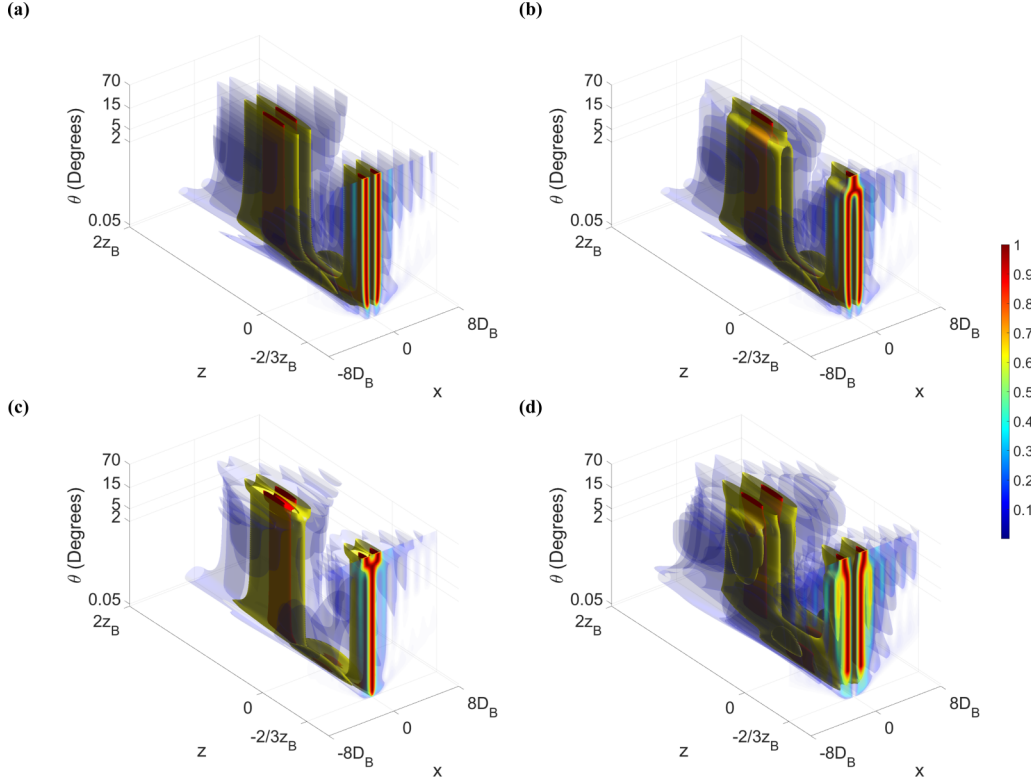
FIG. 2. Distribution of the electric-field intensity in the xz-plane for different values of half-angles θ_B for (a) $\boldsymbol{M}_{BG}^0$, (b) $\boldsymbol{N}_{BG}^0$, (c) $\boldsymbol{N}_{BG}^1$, and (d) $\boldsymbol{N}_{BG}^2$. The wave vector is $k = 2\pi$ and the waist of the Gaussian envelope is $d_0 = 100$. 90% of peak intensity is represented by the red colored isosurface, 50% is represented by the yellow color, and 10% is represented by the blue color. The scale is piecewise linear, the increment between pieces is adjusted to highlight the structure of the beam. The point $z = 0$ is not at the center to showcase the cross section at one particular negative value $z = -2/3z_B$.

IV. VECTOR BESSEL-GAUSSIAN BEAMS

In this section, we investigate the finite-energy versions of spherically polarized Bessel beams. To calculate the components of the vector Bessel-Gaussian beam, the scalar Bessel-Gaussian beam (2) is written as a product of three expressions:

$$E(\rho, \varphi, z, t) = f_1(z)f_2(\rho, z)e^{im\varphi - i\omega t}, \quad (10)$$

where $f_2(\rho, z)$ contains second and third multiplicands in (2) and $f_1(z)$ is all remaining that depend on z.

Thus, the components of vector Bessel-Gaussian beams are expressed in functions $f_1(z) \equiv f_1$ and $f_2(\rho, z) \equiv f_2$ and their derivatives are given in the Appendix. Components of the electric-field mode TE of vector Bessel-Gaussian beam in cylindrical coordinates are

$$\begin{bmatrix} M_\rho \\ M_\varphi \\ M_z \end{bmatrix} = e^{im\varphi - i\omega t} \begin{bmatrix} izmf_1f_2/\rho \\ [f_1(\rho f'_{2z} - zf'_{2\rho}) + \rho f'_1 f_2] \\ -imf_1f_2 \end{bmatrix}. \quad (11)$$

We start with a demonstration of the influence the half-angle of the Bessel cone has on the total intensity profile in one plane. The intensity distribution in the whole space can be obtained by taking the cross section at one particular value of θ_B and rotating it around the z axis. We use the previously discussed considerations, see Sec. II, and limit the half-cone angle θ_B at $\theta_B < 70°$. Although the use of Eq. (2) will not give the exact expressions satisfying the wave equation, the end result will be a good enough approximation [66]. We have validated our choice by calculating the paraxiality estimator [70] for the values we investigate.

The field distribution of the TE mode for the topological charge $m = 0$ is presented in Fig. 2(a). In this case, we observe that, for larger values of the angle θ_B, the intensity distribution scales linearly with the z_B and D_B. Only at large values of θ_B is the side structure observed. For small values of the half-angle θ_B, the structure of the beam undergoes serious changes: the hollow core disappears.

Expressions for the TM mode are obtained as

$$\begin{bmatrix} N_\rho \\ N_\varphi \\ N_z \end{bmatrix} = \frac{e^{im\varphi - i\omega t}}{k\rho} \begin{bmatrix} f_1(m^2 f_2 + \rho f'_{2\rho} - \rho^2 f''_{2zz} + \rho z f''_{2\rho z}) + f'_1(\rho z f'_{2\rho} - 2\rho^2 f'_{2z}) - \rho^2 f''_1 f_2 \\ f_1(zm^2 f_2/\rho - zf'_{2\rho} + 2\rho f'_{2z} z + \rho^2 f''_{2z\rho} - z\rho f''_{2\rho\rho}) + f'_1(2\rho f_2 + \rho^2 f'_{2\rho}) \\ f_1(zm^2 f_2/\rho - zf'_{2\rho} + 2\rho f'_{2z} z + \rho^2 f''_{2z\rho} - z\rho f''_{2\rho\rho}) + f'_1(2\rho f_2 + \rho^2 f'_{2\rho}) \end{bmatrix}. \quad (12)$$

Here, derivatives of functions f_1 and f_2 are explicitly given in the Appendix.
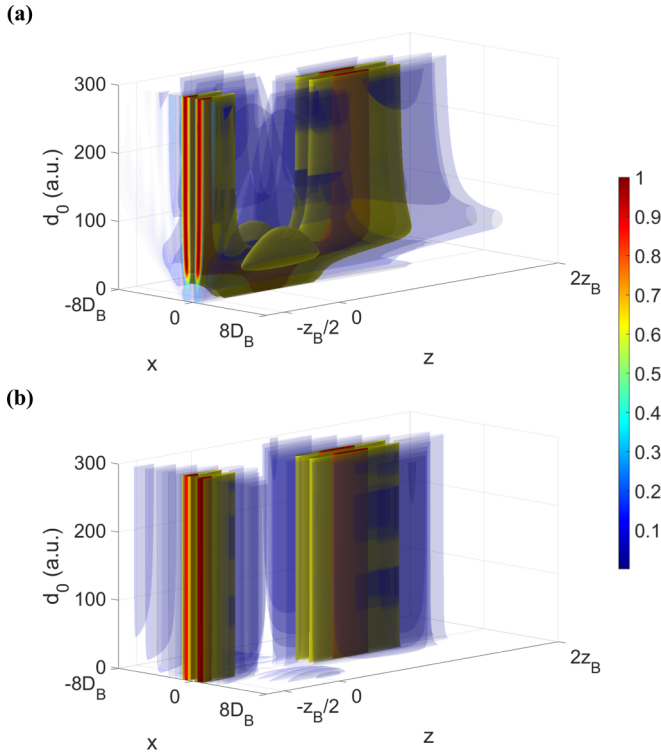
(a)

(b)

FIG. 3. Distribution of the electric-field intensity in the x-z plane for different values of Gaussian envelope waist d_0. The spherically polarized Bessel beam is N_{BG}^0 with the half-cone angle (a) $\theta_B = 1°$, (b) $\theta_B = 15°$. The wave vector is $k = 2\pi$. The scale is piecewise linear, the increment between pieces is adjusted to highlight the structure of the beam. The point $z = 0$ is not at the center to showcase the cross section at one particular negative value $z = -z_B/2$.

The field distribution of the TM mode for the same topological charge is depicted in Fig. 2(b). In this case, the longitudinal component E_z is present, as the half-angle θ_B of the Bessel cone increases, it even becomes dominant. This can be easily noticed from Fig. 2(b). The hollow structure is filled by the electric-field component E_z. Thus, the field structure changes three times as the angle increases.

For this reason, in our next examples, we demonstrate the influence of the topological charge only for the TM mode. In Fig. 2(c) a typical situation for the topological charge $m = 1$ is presented. As we have noted in the previous section, the on-axis polarization state is circular, see Fig. 2(c). No hollow core is observed until the longitudinal component starts to dominate at larger values of θ_B.

Our last example showcases the field distribution of the TM mode for the topological charge $m = 2$, see Fig. 2(d). In this case, the structure of the electric-field intensity undergoes also three times. However, the hollow structure is preserved with the only difference being in the absence of linear scaling and respect to z_B and D_B.

Next, we choose the value of the topological charge $m = 0$ and investigate the influence of the Gaussian envelope d_0 on the intensity distribution of the electric field for the TM mode, see Fig. 3. In the first picture [Fig. 3(a)], the half-cone angle θ_B is small. We observe rather rich and complex changes. For smaller values of the width of the envelope, an appear-

ance of side lobes is observed and the length of the Bessel zone is decreased. This is a natural outcome because the same happens for conventional Bessel beams. This situation is caused by the Rayleigh length of the corresponding beam being smaller than the Bessel zone for this particular angle. As the width d_0 increases we observe more-or-less linear scaling in respect to the constants z_B and D_B. In the second case [see Fig. 3(b)], the value of angle θ_B is larger. For this reason, the length of the Bessel zone is smaller and we do not observe the aforementioned situation for the values of d_0, which we plot. The choice of normalization constants z_B and D_B is clearly proper, because the scale of the beam is invariant to the half-cone angle θ_B and the Gaussian envelope width d_0.

As the choice for the presentation of electric-field intensity distributions might be complicated for the inexperienced eye, we additionally present cross sections of the TM mode for one particular value of $d_0 = 100$ and topological charges $m = 0$, 1, 2, 3 (see Fig. 4). Here, a variety of structures is possible for different values of angle θ_B, this is clearly seen in Fig. 5. In all cases we observe three main changes in the structure which additionally can be subdivided into five cases (see Fig. 4). For small angles in the case of $m = 1$, see Fig. 4(b), the field structure clearly reassembles an optical bottle, which slowly transforms into a double optical needle. As the angle reaches 70°, this double-needle additionally separates transversally and resembles double hollow optical cylinder. For the topological charge of $m = 0$, see Fig. 4(a), the field structure for small angles is rather simple. However, as the angle increases, the beam transforms into a bottle-like structure, which slowly disappears as the angle is further increased. The two last cases, see Figs. 4(c) and 4(d), are more-or-less similar with the case of a larger topological charge undergoing the same changes for larger values of the angle.

The transverse intensity distribution for one example is depicted in, see Fig. 5. Here, not only the total intensity of the electric field is plotted but also its individual constituents. We see that the field structure in this cross section is symmetric and typical for vector type Bessel beams.

V. THE SPATIAL SPECTRUM OF BESSEL-GAUSSIAN VECTOR BEAMS

For the experimental realization of spherically polarized Bessel-Gaussian beams, it is crucial to investigate the properties of the spatial spectra. The spatial spectrum of the vector Bessel-Gaussian beam is obtained as follows: The general expression for the scalar electric field E is

$$E(x, y, z) = \iint_{-\infty}^{+\infty} g(k_x, k_y) e^{ik_x x + ik_y y + ik_z z} dk_x \, dk_y, \quad (13)$$

where $g(k_x, k_y)$ is a spatial spectra of a scalar Bessel-Gaussian beam, see Eq. (3). Now we use Eq. (5) to obtain

$$\begin{aligned} \boldsymbol{L}(x, y, z) &= \boldsymbol{\nabla} E(x, y, z) \\ &= \iint_{-\infty}^{+\infty} g(k_x, k_y) i e^{i(k_x x + k_y y + k_z z)} \\ &\quad \times (\hat{\boldsymbol{e}}_x k_x + \hat{\boldsymbol{e}}_y k_y + \hat{\boldsymbol{e}}_z k_z) dk_x \, dk_y, \quad (14) \end{aligned}$$

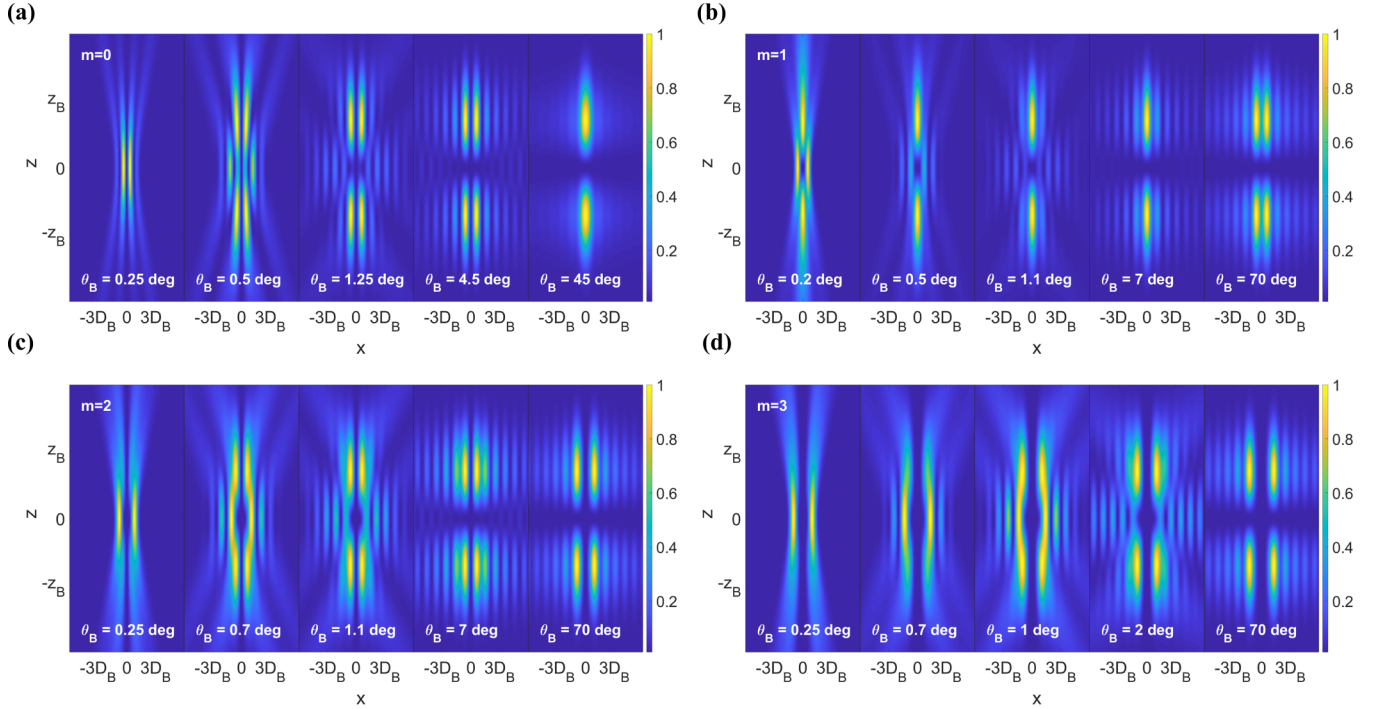FIG. 4. Distribution of the electric-field intensity in the x-z plane for different values of topological charge m and half-cone angles θ_B in the cross section of the N_{BG}^0 beam. The values of half-cone angles are given in the subplots and the values of the topological charge m are (a) $m = 0$, (b) $m = 1$, (c) $m = 2$, (d) $m = 3$. The intensity maximum is normalized to the peak maximum of the beam. The wave vector is $k = 2\pi$, the waist of the Gaussian envelope is $d_0 = 100$, and the Bessel half-cone angle is $\theta_B = 1°$.

As a next step, we multiply Eq. (14) by $\mathbf{R}$ to obtain the TE mode in terms of scalar Bessel-Gaussian spectra

$$\mathbf{M}_{BG}(x, y, z)|_{z=0} = \iint_{-\infty}^{+\infty} g(k_x, k_y) i e^{i\mathbf{k} \cdot \mathbf{R}} [-\hat{\mathbf{e}}_x y k_z$$
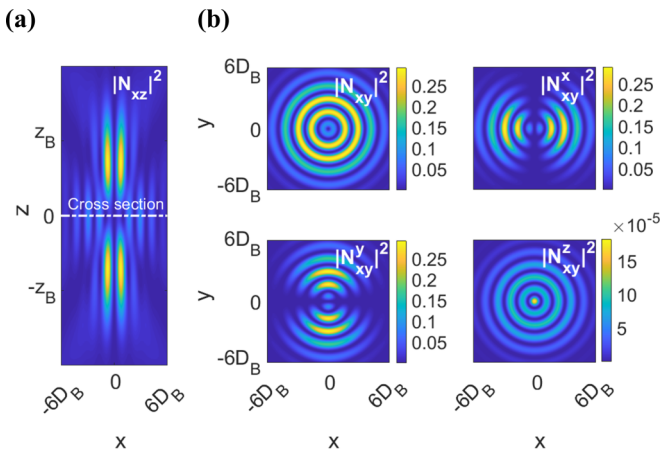$$+ \hat{\mathbf{e}}_y x k_z + \hat{\mathbf{e}}_z (y k_x - x k_y)] dk_x \, dk_y, \quad (15)$$

FIG. 5. Distribution of the intensities for the total and individual components (marked in subplots) of the electric field in various planes for the beam N_{BG}^0 ($m = 0$). The longitudinal plane x, z is presented in panel (a), the transverse plane is depicted in panel (b). The intensity maximum is normalized to the peak maximum of the beam. The wave vector is $k = 2\pi$, the waist of the Gaussian envelope is $d_0 = 100$, and the Bessel half-cone angle is $\theta_B = 1°$.

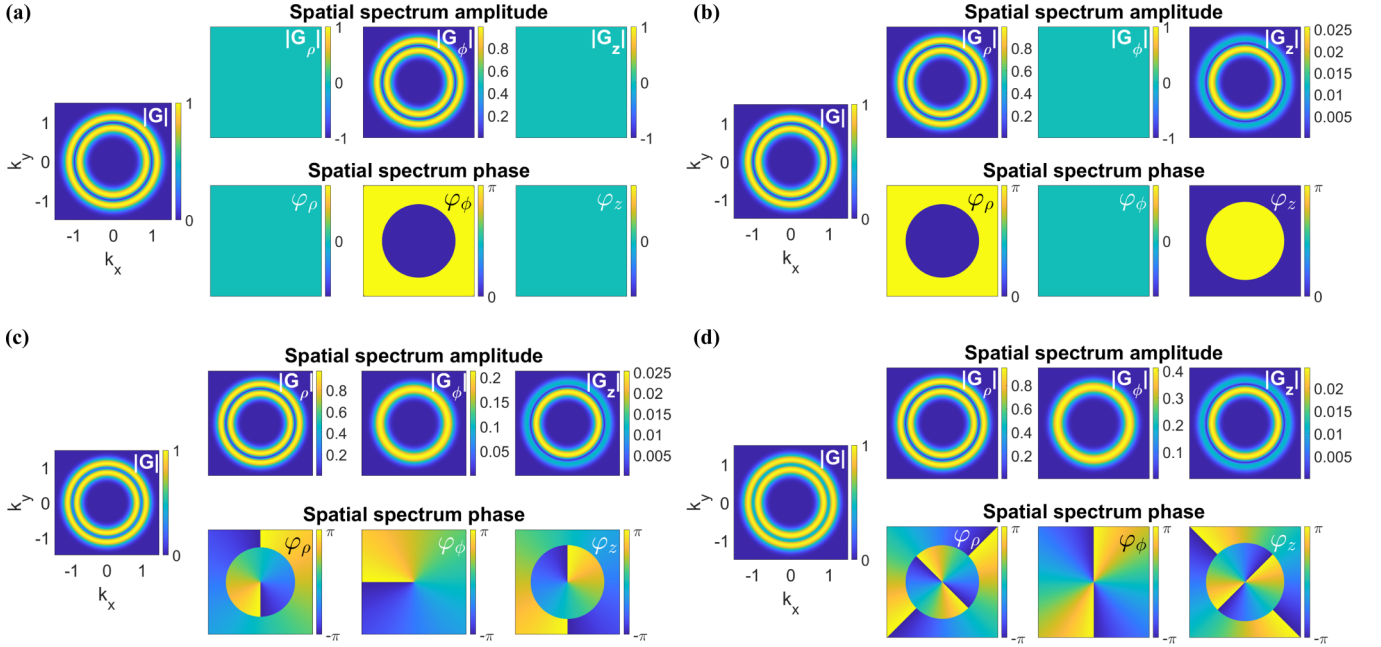We use the Fourier transform of the Eq. (15) and derive the spatial spectrum of TE mode of the vector Bessel-Gaussian beam

$$\mathbf{G}_{BG}^M(k_x, k_y) = \frac{1}{4\pi^2} \iint_{-\infty}^{+\infty} \mathbf{M}(x, y, 0) \, e^{-i(k_x' x + k_y' y)} dx \, dy, \quad (16)$$

Combination of Eqs. (15) and (16) is quite lengthy. For this reason, we present only the derivation for one of the components. As the other components are obtained in the same manner. The spectral x component of the TM mode of the vector Bessel-Gaussian beam is

$$G_{BG}^M(k_x', k_y')_x = -\frac{1}{4\pi^2} \iiiint_{-\infty}^{+\infty} g(k_x, k_y) i e^{i(k_x - k_x')x}$$
$$\times e^{i(k_y - k_y')y} \, y \, k_z \, dx \, dy \, dk_x \, dk_y, \quad (17)$$

where $k_z = (k^2 - k_x^2 - k_y^2)^{1/2}$ is the z component of the wave vector. Equation (17) is analytically expressible as follows:

$$G_{BG}^M(k_x', k_y')_x = -\frac{\partial}{\partial k_y'} \left[g(k_x', k_y') \sqrt{k^2 - k_x'^2 - k_y'^2} \right], \quad (18)$$

The same procedure gives expressions for the spectral y and z components of $\mathbf{G}_{BG}^M(k_x, k_y)$, see Eq. (16), so we get

$$\mathbf{G}_{BG}^M(k_x, k_y) = \begin{bmatrix} -\frac{\partial}{\partial k_y} \left[g(k_x, k_y) \sqrt{k^2 - k_x^2 - k_y^2} \right] \\ \frac{\partial}{\partial k_x} \left[g(k_x, k_y) \sqrt{k^2 - k_x^2 - k_y^2} \right] \\ k_x \frac{\partial}{\partial k_y} g(k_x, k_y) - k_y \frac{\partial}{\partial k_x} g(k_x, k_y) \end{bmatrix}. \quad (19)$$

FIG. 6. Distributions of the amplitudes and phases for spherically polarized vector Bessel-Gaussian vortex beams (a) M_{BG}^0, (b) N_{BG}^0, (c) N_{BG}^1, and (d) N_{BG}^2. All individual components of the spatial spectrum are presented in the cylindrical coordinate system (individual amplitudes are $|G_\rho|$, $|G_\phi|$, $|G_z|$, individual phases are φ_ρ, φ_ϕ, φ_z). The wave vector is $k = 2\pi$, the waist of Gaussian envelope $d_0 = 100$, and the Bessel half-cone angle is $\theta_B = 1°$. The topological charges are (a), (b) $m = 0$, (c) $m = 1$, (d) $m = 2$. The first picture in each group is the amplitude of the whole spatial spectrum, the spatial coordinates in all groups are the same as in the first picture of the group.

The spatial spectrum of the vector Bessel-Gaussian beam in this case with different topological numbers is depicted in Fig. 6(a). The spatial spectrum of the scalar Bessel-Gaussian beam see Eq. (3) is a ring, however, the spatial spectrum of the vector Bessel-Gaussian beam is mathematically obtained by performing differentiation in respect to k_x and k_y coordinates. For this reason, a two-ring structure appears, see Fig. 6(a). In the first case, no G_ρ and no G_z component is present. The G_ϕ component is a two-ring structure with a phase jump appearing between rings.

Next, we repeat the derivations in Eqs. (15)–(19), but apply them for the expression for the TM mode N_{BG}. Its spatial spectra $G_{BG}^N(k_x, k_y)$ can be expressed as

$$G_{BG}^N(k_x, k_y) = \frac{i}{k} \begin{bmatrix} 2g(k_x, k_y)k_x - \frac{\partial}{\partial k_x}\left[g(k_x, k_y)\left(k_z^2 + k_y^2\right)\right] + \frac{\partial}{\partial k_y}\left[g(k_x, k_y)k_x k_y\right] \\ 2g(k_x, k_y)k_y + \frac{\partial}{\partial k_x}\left[g(k_x, k_y)k_x k_y\right] - \frac{\partial}{\partial k_y}\left[g(k_x, k_y)(k_z^2 + k_x^2)\right] \\ 2g(k_x, k_y)k_z + \frac{\partial}{\partial k_x}\left[g(k_x, k_y)k_x k_z\right] + \frac{\partial}{\partial k_y}\left[g(k_x, k_y)k_y k_z\right] \end{bmatrix},$$

Here our analysis focuses on the selected cases showcased previously, see Figs. 4(b)–4(d). Topological charges once again are $m = 0$ in Fig. 6(b). First, because of the transversality of the magnetic field, we observe the disappearance of the G_ϕ component, but the other two components G_ρ and G_z appear. They share the same distinct two-ring structure. The G_ρ and G_z components are π out of phase. This situation is known in the literature when highly confined fields are analyzed [71].

In Fig. 6(c), the topological charge is $m = 1$. In this case, the G_ϕ component is nonzero, the amplitude is a single ring with the topological vortex of charge $m = 1$ present. The other two components are still out of phase and the topological vortices do appear there also. The intensity profile is the same two-ring structure.

Lastly, in Fig. 6(d), the topological charge is $m = 2$. The situation here is similar to the previous case—the intensity profiles are similar. However, as expected, for the phases of G_ρ and G_z we observe phase jumps between the rings when the topological charges are increased to $m = 2$.

To this end, we investigate how different half-cone angles θ_B and Gaussian envelope widths d_0 are influencing the spatial spectra of TE and TM modes. This interplay is expected to rebalance the ratio between the G_z and other components as the half-angle of the cone determines whether the vector Bessel-Gaussian beam is in the paraxial regime when the G_z component is very small or in the nonparaxial regime when the G_z component is dominant. The result of this investigation is presented in Fig. 7.
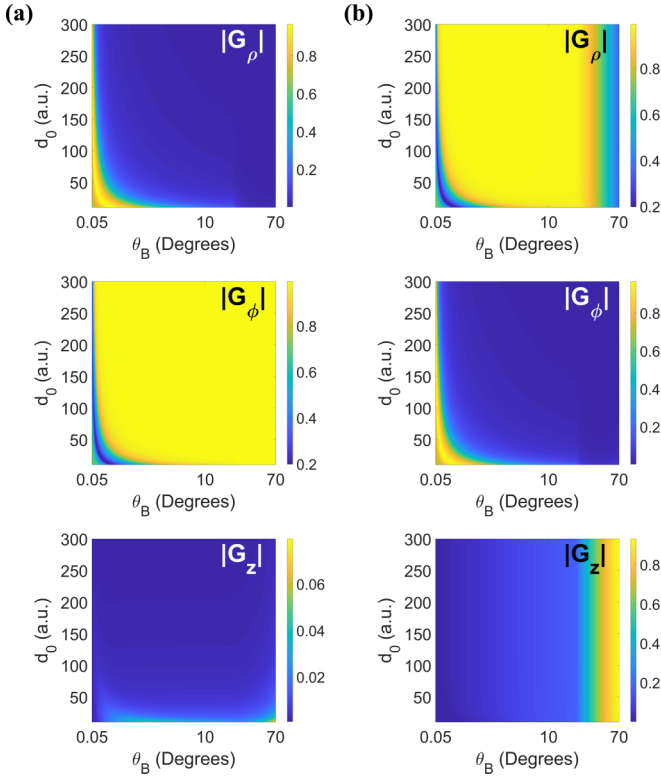
FIG. 7. Depiction of the dependency of integrated individual spectral amplitudes on the half-cone angle θ_B and widths d_0 of Gaussian envelope for (a) M_{BG}^1 and (b) N_{BG}^1. The topological charge is $m = 1$, the integration was performed over the whole spectral plane and the individual amplitudes are normalized to the total amplitude.

First, in Fig. 7(a), three different integrated spectral plane spectral components of the TE mode with topological charge $m = 1$ are presented. In this case, the G_z component is negligibly small and has no influence on the beam structure. However, the changes in half-cone angle and widths of the envelope redistribute the energy between G_ρ and G_ϕ components. In the paraxial regime, for very small angles, θ_B the G_ρ dominates. Nevertheless, this region is characteristic only for small angles and widths. In other cases, the G_ϕ component contains the largest energy.

Lastly, in Fig. 7(b), the TM mode with topological charge $m = 1$ is investigated. As expected, with the increase of the half-cone angle θ_B the G_z component starts to dominate in the region $\theta_B > 1$ rad. For smaller values of the half-cone angle, the situation observed in the previous case is repeated. However, for small angles and small widths of the envelope, the G_ϕ component is larger than the G_ρ component. As the angles and widths are increasing the energy is rapidly redistributed from the G_ϕ component to G_ρ component.

VI. CONCLUSIONS

Spherically polarized vector Bessel vortices were introduced. In contrary to the already known polarization states (linear, circular, radial, and azimuthal), these polarization singularities are one dimensional and thus modify the axial intensity profile of the Bessel beams. The transverse electric state can be characterized as a combination of azimuthally and meridionally dependent electric-field orientations. The transverse magnetic polarization state is predominantly oriented along the radius vector of the spherical coordinates.

Spherically polarized vector Bessel vortices can be represented on the hybrid Poincaré sphere as a complexly evolving set of points corresponding to the different locations in the real 3D space. An exact description of a spherically polarized Bessel vortex requires an introduction of the 3D Stokes parameters [44].

Although the scalar Bessel vortices have a nonzero topological charge associated with orbital angular momentum, the spherically polarized Bessel vortices have topological charges which are smaller due to the conversion of orbital angular momentum into the spin angular momentum.

In the case of spherically polarized Bessel-Gaussian beams, rather complicated structures can be observed depending on the values of the half-cone angles and the widths of the Gaussian envelope. For the transverse electric beams, we observe two regimes: low angle and high angle. Surprisingly, the transverse magnetic beam undergoes structural changes three times as we change the half-cone angle.

The spatial spectrum is quite complicated with all three spatial components (x, y, z) present. However, in the cylindrical coordinates expressions are simplified and some spectral components are not present.

Our investigation has revealed a large variety of different topologies appearing in the spherically polarized Bessel vortices as the angle of the half-cone θ_B interplays with the width d_0 of the Gaussian envelope. We did observe an appearance of optical bottles [59,72], needles, [4,62,73], and doughnuts [49–51]. Such rich structural properties are becoming important as structured light is increasingly employed in imaging [74], super-resolution [75], maximal energy concentration [76], particle [77,78] and atom trapping [79,80], and laser microprocessing [81].

APPENDIX

Functions $f_1(z)$ and $f_2(z, \rho)$ [see Eq. (10)] are

$$f_1(z) = \frac{1}{Z} \exp\left(-i\frac{k_\rho^2}{2k}\frac{z}{Z}\right) \exp\left(-ik_z z\right), \quad \text{(A1)}$$

$$f_2(z, \rho) = J_m\left(\frac{k_\rho \rho}{Z}\right) \exp\left(-\frac{\rho^2}{d_0^2 Z}\right). \quad \text{(A2)}$$

For simplicity, the argument of Bessel function is omitted: $J_{m-1} \equiv J_{m-1}(k_\rho \rho / Z)$. Expressions for the derivatives of functions f_1 are as follows:

$$f_1'(z) = \exp\left(-i\frac{k_\rho^2}{2k}\frac{z}{Z} + ikz\right)$$

$$\times \left(\frac{ik}{Z} - \frac{i}{z_0 Z^2} - \frac{ik_\rho^2}{2kZ^2} - \frac{zk_\rho^2}{2kz_0 Z^3}\right), \quad \text{(A3)}$$

$$f_1''(z) = \exp\left(-i\frac{k_\rho^2}{2k}\frac{z}{Z} + ikz\right)\left(\frac{(z+iZz_0)^2k_\rho^4}{4k^2Z^5z_0^2} - \frac{2}{Z^3z_0^2}\right.$$
$$\left. -\frac{k^2}{Z} + \frac{2izk_\rho^2}{kZ^4z_0^2} + \frac{2kk_\rho^2}{Z^4z_0} - \frac{2k_\rho^2}{kZ^3z_0} - \frac{izk_\rho^2}{Z^3z_0}\right). \quad (A4)$$

First-order derivatives of functions f_2 are

$$f_2'(\rho,z)_z = -iG\left(\frac{k_\rho\rho}{z_0Z^2}J_{m-1} - AJ_m\right), \quad (A5)$$

$$f_2'(\rho,z)_\rho = G\left(\frac{k_\rho}{Z}J_{m-1} - BJ_m\right). \quad (A6)$$

Second-order derivatives of functions f_2 are

$$f_2''(\rho,z)_{zz} = G\left[\left(\frac{2k_\rho\rho^3}{z_0^2d_0^2Z^4} - \frac{k_\rho\rho}{z_0^2Z^3}\right)J_{m-1}\right.$$
$$\left. + \left(\frac{k_\rho^2\rho^2}{z_0^2Z^4} + \frac{2\rho^2}{z_0^2d_0^2Z^3} + \frac{m}{z_0^2Z^2} - A^2\right)J_m\right], \quad (A7)$$

$$f_2''(\rho,z)_{\rho\rho} = -G\left[\left(\frac{4\rho k_\rho}{d_0^2Z^2} + \frac{k_\rho}{\rho Z}\right)J_{m-1}\right.$$
$$\left. - \left(\frac{m}{\rho^2} - \frac{2}{d_0^2Z} - \frac{k_\rho^2}{Z^2} + B^2\right)J_m\right], \quad (A8)$$

$$f_2''(\rho,z)_{z\rho} = f_2''(\rho,z)_{\rho z}$$
$$= iG\left[\frac{3k_\rho\rho^2}{z_0d_0^2Z^3}J_{m-1} + \left(\frac{k_\rho^2\rho}{z_0Z^3} + \frac{2\rho}{z_0d_0^2Z^2} - AB\right)J_m\right], \quad (A9)$$

where

$$G = \exp\left(-\frac{\rho^2}{d_0^2Z}\right), \quad (A10)$$

$$A = \left(\frac{\rho^2}{z_0d_0^2Z^2} + \frac{m}{z_0Z}\right),$$

$$B = \left(\frac{2\rho}{d_0^2Z} + \frac{m}{\rho}\right).$$

[1] J. Durnin, J. Opt. Soc. Am. A **4**, 651 (1987).

[2] J. Durnin, J. J. Miceli, Jr., and J. H. Eberly, Phys. Rev. Lett. **58**, 1499 (1987).

[3] S. N. Khonina, N. L. Kazanskiy, S. V. Karpeev, and M. A. Butt, Micromachines **11**, 997 (2020).

[4] R. Grunwald and M. Bock, Adv. Phys.: X **5**, 1736950 (2020).

[5] J. C. Gutiérrez-Vega, M. Iturbe-Castillo, and S. Chávez-Cerda, Opt. Lett. **25**, 1493 (2000).

[6] P. Slevas, S. Orlov, E. Nacius, O. Ulcinas, P. Gotovski, J. Baltrukonis, and V. Jukna, in *Laser Applications in Microelectronic and Optoelectronic Manufacturing (LAMOM) XXV* (International Society for Optics and Photonics, 2020), Vol. 11267, p. 112670B.

[7] M. A. Bandres and B. Rodríguez-Lara, New J. Phys. **15**, 013054 (2013).

[8] S. Orlov, V. Vosylius, P. Gotovski, A. Grabusovas, J. Baltrukonis, and T. Gertus, J. Laser Micro Nanoeng. **13**, 280 (2018).

[9] J. A. Stratton, *Electromagnetic Theory* (John Wiley & Sons, 2007), Vol. 33.

[10] Z. Bouchal and M. Olivík, J. Mod. Opt. **42**, 1555 (1995).

[11] R. Dorn, S. Quabis, and G. Leuchs, Phys. Rev. Lett. **91**, 233901 (2003).

[12] S. Quabis, R. Dorn, M. Eberler, O. Glöckl, and G. Leuchs, Opt. Commun. **179**, 1 (2000).

[13] Y. Zhang, L. Wang, and C. Zheng, J. Opt. Soc. Am. A **22**, 2542 (2005).

[14] Y. Kozawa and S. Sato, J. Opt. Soc. Am. A **24**, 1793 (2007).

[15] L. Novotny and B. Hecht, *Principles of Nano-Optics* (Cambridge University Press, New York, 2012).

[16] E. Heyman, B. Steinberg, and L. Felsen, J. Opt. Soc. Am. A **4**, 2081 (1987).

[17] J.-Y. Lu and J. F. Greenleaf, IEEE Trans. Ultrson. Ferroelectr. Freq. Control **39**, 19 (1992).

[18] S. Orlov, A. Piskarskas, and A. Stabinis, Opt. Lett. **27**, 2167 (2002).

[19] S. Orlov and A. Stabinis, Opt. Commun. **240**, 1 (2004).

[20] P. Saari and K. Reivelt, Phys. Rev. Lett. **79**, 4135 (1997).

[21] N. Chiotellis, V. Mendez, S. M. Rudolph, and A. Grbic, Phys. Rev. B **97**, 085136 (2018).

[22] A. Ciattoni, C. Conti, and P. Di Porto, Phys. Rev. E **69**, 036608 (2004).

[23] P. Gotovski and S. Orlov, J. Laser Micro Nanoeng. **14**, 25 (2019).

[24] V. Vosylius and S. Orlov, J. Laser Micro Nanoeng. **14**, 74 (2019).

[25] M. Soskin and M. Vasnetsov, Prog. Opt. **42**, 219 (2001).

[26] I. Freund, Opt. Commun. **201**, 251 (2002).

[27] V. V. Kotlyar, S. S. Stafeev, and A. G. Nalimov, Phys. Rev. A **99**, 033840 (2019).

[28] E. Otte and C. Denz, Opt. Lett. **43**, 5821 (2018).

[29] T. Bauer, P. Banzer, E. Karimi, S. Orlov, A. Rubano, L. Marrucci, E. Santamato, R. W. Boyd, and G. Leuchs, Science **347**, 964 (2015).

[30] K. Tekce, E. Otte, and C. Denz, Opt. Express **27**, 29685 (2019).

[31] J. Kreismann and M. Hentschel, Europhys. Lett. **121**, 24001 (2018).

[32] S. Orlov and J. Berškys, J. Quant. Spectrosc. Radiat. Transfer **261**, 107490 (2021).

[33] A. Aiello, P. Banzer, M. Neugebauer, and G. Leuchs, Nat. Photonics **9**, 789 (2015).

[34] A. Chong, C. Wan, J. Chen, and Q. Zhan, Nat. Photonics **14**, 350 (2020).

[35] T. Bauer, P. Banzer, F. Bouchard, S. Orlov, L. Marrucci, E. Santamato, R. W. Boyd, E. Karimi, and G. Leuchs, New J. Phys. **21**, 053020 (2019).

[36] K. Y. Bliokh, M. A. Alonso, and M. R. Dennis, Rep. Prog. Phys. **82**, 122401 (2019).

[37] Ruchi, P. Senthilkumaran, and S. K. Pal, Int. J. Opt. **2020**, 2812803 (2020).

[38] I. Moreno, J. A. Davis, I. Ruiz, and D. M. Cottrell, Opt. Express **18**, 7173 (2010).

[39] M. R. Dennis, R. P. King, B. Jack, K. O'holleran, and M. J. Padgett, Nat. Phys. **6**, 118 (2010).

[40] J. Leach, M. R. Dennis, J. Courtial, and M. J. Padgett, New J. Phys. **7**, 55 (2005).

[41] M. J. Padgett and J. Courtial, Opt. Lett. **24**, 430 (1999).

[42] X. Yi, Y. Liu, X. Ling, X. Zhou, Y. Ke, H. Luo, S. Wen, and D. Fan, Phys. Rev. A **91**, 023801 (2015).

[43] G. Milione, H. I. Sztul, D. A. Nolan, and R. R. Alfano, Phys. Rev. Lett. **107**, 053601 (2011).

[44] C. J. R. Sheppard, Phys. Rev. A **90**, 023809 (2014).

[45] M. Rose, *Multipole Fields* (John Wiley & Sons, 1955).

[46] S. Orlov and U. Peschel, Phys. Rev. A **82**, 063820 (2010).

[47] S. Orlov and P. Banzer, Phys. Rev. A **90**, 023832 (2014).

[48] S. Orlov and J. Berškys, Phys. Rev. A **102**, 063532 (2020).

[49] M. E. J. Friese, J. Enger, H. Rubinsztein-Dunlop, and N. R. Heckenberg, Phys. Rev. A **54**, 1593 (1996).

[50] B. J. Roxworthy and K. C. Toussaint, Jr., New J. Phys. **12**, 073012 (2010).

[51] Q. Zhan and J. R. Leger, Opt. Express **10**, 324 (2002).

[52] N. Simpson, K. Dholakia, L. Allen, and M. Padgett, Opt. Lett. **22**, 52 (1997).

[53] J. R. Moffitt, Y. R. Chemla, S. B. Smith, and C. Bustamante, Annu. Rev. Biochem. **77**, 205 (2008).

[54] K. Gahagan and G. Swartzlander, J. Opt. Soc. Am. B **16**, 533 (1999).

[55] P. J. Rodrigo, V. R. Daria, and J. Glückstad, Opt. Express **12**, 1417 (2004).

[56] M. Woerdemann, *Structured Light Fields: Applications in Optical Trapping, Manipulation, and Organisation* (Springer Science & Business Media, 2012).

[57] G. D. Jeffries, J. S. Edgar, Y. Zhao, J. P. Shelby, C. Fong, and D. T. Chiu, Nano Lett. **7**, 415 (2007).

[58] T. T. Perkins, Laser Photonics Rev. **3**, 203 (2009).

[59] J. Arlt and M. J. Padgett, Opt. Lett. **25**, 191 (2000).

[60] Y. Xiao, Z. Yu, R. A. Wambold, H. Mei, G. Hickman, R. H. Goldsmith, M. Saffman, and M. A. Kats, Nanophot. **10**, 2893 (2021).

[61] S. Orlov, A. Gajauskaitė, and A. Grabusovas, J. Laser Micro Nanoeng. **13**, 223 (2018).

[62] E. T. Rogers, S. Savo, J. Lindberg, T. Roy, M. R. Dennis, and N. I. Zheludev, Appl. Phys. Lett. **102**, 031108 (2013).

[63] V. Jarutis, R. Paškauskas, and A. Stabinis, Opt. Commun. **184**, 105 (2000).

[64] M. Lax, W. H. Louisell, and W. B. McKnight, Phys. Rev. A **11**, 1365 (1975).

[65] R. Borghi, M. Santarsiero, and M. A. Porras, J. Opt. Soc. Am. A **18**, 1618 (2001).

[66] P. Vaveliuk, G. F. Zebende, M. A. Moret, and B. Ruiz, J. Opt. Soc. Am. A **24**, 3297 (2007).

[67] S. Orlov, K. Regelskis, V. Smilgevičius, and A. Stabinis, Opt. Commun. **209**, 155 (2002).

[68] P. M. Morse and H. Feshbach, *Methods of Theoretical Physics* (McGraw-Hill, New York, 1953).

[69] See Supplemental Material at http://link.aps.org/supplemental/10.1103/PhysRevA.105.013502 for an animated depiction of three normalized Stokes parameters representing $\boldsymbol{M}_B^1$ add $\boldsymbol{N}_B^1$ for different points in the x, z plane for different values of θ_B.

[70] P. Vaveliuk, B. Ruiz, and A. Lencina, Opt. Lett. **32**, 927 (2007).

[71] T. Bauer, S. Orlov, U. Peschel, P. Banzer, and G. Leuchs, Nat. Photonics **8**, 23 (2014).

[72] I. Chremmos, P. Zhang, J. Prakash, N. K. Efremidis, D. N. Christodoulides, and Z. Chen, Opt. Lett. **36**, 3675 (2011).

[73] J. Wang, W. Chen, and Q. Zhan, Opt. Express **18**, 21965 (2010).

[74] Y. Yan, L. Li, C. Feng, W. Guo, S. Lee, and M. Hong, ACS Nano **8**, 1809 (2014).

[75] E. T. Rogers and N. I. Zheludev, J. Opt. (Bristol, U. K.) **15**, 094008 (2013).

[76] H. Shim, H. Chung, and O. D. Miller, Phys. Rev. Appl. **14**, 014007 (2020).

[77] D. G. Grier, Nature (London) **424**, 810 (2003).

[78] M. Kunitski, N. Eicke, P. Huber, J. Köhler, S. Zeller, J. Voigtsberger, N. Schlott, K. Henrichs, H. Sann, F. Trinter, L. P. H. Schmidt, A. Kalinin, M. S. Schöffler, T. Jahnke, M. Lein, and R. Dörner, Nat. Commun. **10**, 1 (2019).

[79] P. Xu, X. He, J. Wang, and M. Zhan, Opt. Lett. **35**, 2164 (2010).

[80] D. Barredo, V. Lienhard, P. Scholl, S. de Léséleuc, T. Boulier, A. Browaeys, and T. Lahaye, Phys. Rev. Lett. **124**, 023201 (2020).

[81] M. Malinauskas, A. Žukauskas, S. Hasegawa, Y. Hayasaki, V. Mizeikis, R. Buividas, and S. Juodkazis, Light: Sci. Appl. **5**, e16133 (2016).